LETTER

doi:10.1038/nature15728

The DNA glycosylase AlkD uses a non-base-flipping mechanism to excise bulky lesions

Elwood A. Mullins[1], Rongxin Shi[1], Zachary D. Parsons[1], Philip K. Yuen[2], Sheila S. David[2], Yasuhiro Igarashi[3] & Brandt F. Eichman[1]

Threats to genomic integrity arising from DNA damage are mitigated by DNA glycosylases, which initiate the base excision repair pathway by locating and excising aberrant nucleobases[1,2]. How these enzymes find small modifications within the genome is a current area of intensive research. A hallmark of these and other DNA repair enzymes is their use of base flipping to sequester modified nucleotides from the DNA helix and into an active site pocket[2–5]. Consequently, base flipping is generally regarded as an essential aspect of lesion recognition and a necessary precursor to base excision. Here we present the first, to our knowledge, DNA glycosylase mechanism that does not require base flipping for either binding or catalysis. Using the DNA glycosylase AlkD from *Bacillus cereus*, we crystallographically monitored excision of an alkylpurine substrate as a function of time, and reconstructed the steps along the reaction coordinate through structures representing substrate, intermediate and product complexes. Instead of directly interacting with the damaged nucleobase, AlkD recognizes aberrant base pairs through interactions with the phosphoribose backbone, while the lesion remains stacked in the DNA duplex. Quantum mechanical calculations revealed that these contacts include catalytic charge–dipole and CH–π interactions that preferentially stabilize the transition state. We show *in vitro* and *in vivo* how this unique means of recognition and catalysis enables AlkD to repair large adducts formed by yatakemycin, a member of the duocarmycin family of antimicrobial natural products exploited in bacterial warfare and chemotherapeutic trials[6,7]. Bulky adducts of this or any type are not excised by DNA glycosylases that use a traditional base-flipping mechanism[5]. Hence, these findings represent a new model for DNA repair and provide insights into catalysis of base excision.

Alkylation of DNA by endogenous metabolites, environmental toxins and chemotherapeutic agents is a major source of genotoxic damage[8]. By virtue of their positive charge, *N*3- and *N*7-alkylpurines are prone to spontaneous depurination at physiological pH, and both *N*3-methyladenine (3mA) and apurinic/apyrimidinic (AP) sites interfere with DNA replication and transcription[9,10]. As the initial step in the base excision repair pathway, DNA glycosylases remove 3mA and other cationic and neutral nucleobases from the genome. Both enzymatic and non-enzymatic depurination of these lesions have been shown to proceed through a stepwise pathway initiated by cleavage of the glycosidic bond, followed by addition of the nucleophilic water to the oxocarbenium (dR^+) intermediate[11] (Fig. 1a). The resulting AP site is then converted to an undamaged nucleotide by a common set of lesion-independent base excision repair enzymes[1,2].

Despite their structural diversity, DNA glycosylases are generally thought to accomplish base flipping through the use of two conserved protein elements—a nucleobase binding pocket and a DNA intercalating residue[5]. The nucleobase binding pocket provides a means of damage recognition through shape and charge complementary with the modified base, while also creating a scaffold for the residues that catalyse hydrolysis of the *N*-glycosidic bond. With few exceptions, an aspartate or glutamate residue has a dual role in stabilizing developing positive charge on the sugar as the glycosidic bond is broken and in deprotonating the nucleophilic water that forms the AP product[12]. Additional residues in the pocket enhance the leaving-group potential of the base. For neutral alkylpurines, this enhancement comes from a general acid that protonates the nucleobase to provide the same instability inherent to cationic purines, which are in essence pre-activated for depurination[11]. Outside the binding pocket, DNA intercalating residues stabilize the catalytically active conformation of the DNA by filling the void in the duplex created when the lesion is flipped[13].

We previously determined that the alkylpurine DNA glycosylase AlkD from *B. cereus*[14] uniquely recognizes damaged DNA without a nucleobase binding pocket or an intercalating residue[15,16]. However, the modified nucleotides in these structures were not in contact with the protein, leaving us to only speculate on the catalytic mechanism. To determine how AlkD excises positively charged substrates without a base binding pocket or an intercalating residue, we determined a new AlkD crystal structure with DNA containing 3-deaza-3-methyladenine (3d3mA), a comparatively stable isostere of 3mA (Fig. 1b and Extended Data Table 1). As in the previous AlkD–DNA complexes, the DNA duplex is bound by the concave surface of the protein. The helix is bent by 30° away from the enzyme while the minor groove surrounding the lesion is widened by 4 Å (Fig. 1c). This distortion induces an equilibrium in which the 3d3mA•T base pair is in either a Watson–Crick or highly sheared conformation. Shearing displaces the 3d3mA nucleobase by 4 Å into the minor groove and towards AlkD, but leaves the base partially stacked in the duplex (Extended Data Fig. 1). In this conformation, the deoxyribose of 3d3mA is in contact with three residues—Trp109, Asp113 and Trp187 (Fig. 1d)—all of which are crucial for lesion excision and are invariant in the AlkD family[15–18]. The carboxylate and two indole side chains cradle the backbone of the lesion and the two flanking nucleotides. Asp113 is in line with the *N*-glycosidic bond of 3d3mA and thus ideally positioned to stabilize developing positive charge on the deoxyribose as the nucleobase is excised (Fig. 1d). This arrangement also allows Asp113 to position and deprotonate the nucleophilic water for subsequent addition to the oxocarbenium intermediate. Similar interactions between catalytic carboxylate residues and the deoxyribose are achieved by other DNA glycosylases, but only after the lesion has been flipped into the nucleobase binding pocket. By contrast, hypothetical rotation of the 3d3mA nucleotide in the AlkD complex would disrupt these catalytic contacts. The lack of base flipping, however, precludes a general acid from gaining access to protonate the nucleobase substrate, which limits AlkD to excision of cationic lesions.

Unlike 3mA, 3d3mA is uncharged and therefore refractory to depurination at physiological pH[10]. To our surprise, the electron density in the new AlkD–DNA complexes revealed a mixture of intact 3d3mA nucleotide together with AP site and free 3d3mA nucleobase, indicating that cleavage of the *N*-glycosidic bond had occurred (Fig. 2a and Extended Data Fig. 2). By flash-freezing crystals at various times and determining their structures, we were able to visualize the glycosylase reaction at 1.4–2.0 Å resolution, starting with intact

[1]Department of Biological Sciences and Center for Structural Biology, Vanderbilt University, Nashville, Tennessee 37232, USA. [2]Department of Chemistry, University of California, Davis, California 95616, USA. [3]Biotechnology Research Center, Toyama Prefectural University, 5180 Kurokawa, Imizu, Toyama 939-0398, Japan.

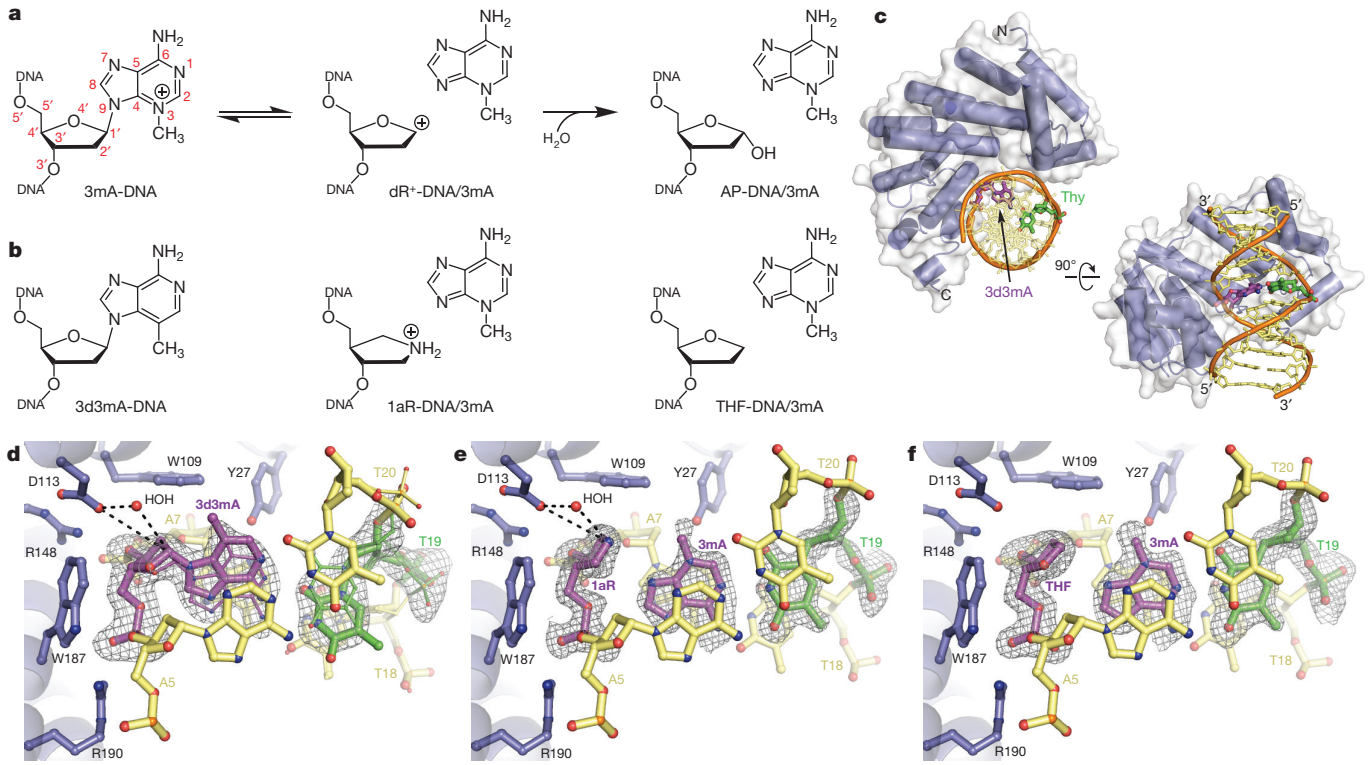

Figure 1 | Crystallographic reconstruction of the reaction trajectory for 3mA excision. a, Proposed reaction scheme illustrating stepwise depurination of 3mA-DNA. **b**, Corresponding structural analogues used for crystallography. **c**, AlkD–3d3mA-DNA complex. **d**, Substrate-like complex containing 3d3mA-DNA. Watson–Crick (56%) and sheared (44%) conformations of the 3d3mA•T base pair are represented with thin and thick bonds, respectively. **e**, Intermediate-like complex containing 1aR-DNA and 3mA nucleobase. **f**, Product-like complex containing THF-DNA and 3mA nucleobase. AlkD is coloured blue, the lesion is purple, the opposing thymine is green and the flanking nucleotides are yellow. Charge–dipole and hydrogen-bonding interactions are shown as dashed lines. Annealed omit electron density in **d**–**f** is contoured to 2.5σ.

3d3mA-DNA substrate and ending with AP-DNA product (Fig. 2a and Extended Data Tables 1 and 2). Quantifying the fractional occupancies of substrate and product over the course of the reaction gave a rate constant for *in crystallo* base excision of $4.6 \times 10^{-6}\,s^{-1}$ (Fig. 2b). For comparison, cationic 3mA lesions are excised by AlkD at least 800-fold more rapidly[19]. The unexpected excision of 3d3mA can be explained by pH-dependent protonation at *N*7, which would confer positive charge on 3d3mA, activating it for excision by AlkD (Fig. 2c). Given the moderately acidic (pH 5.7) crystallization buffer and the calculated pK_a (3.8) of 3d3mA, ~1% of the lesion should be protonated, consistent with the slow rate of *in crystallo* cleavage. By contrast, we did not observe excision of 3d3mA in AlkD–3d3mA-DNA

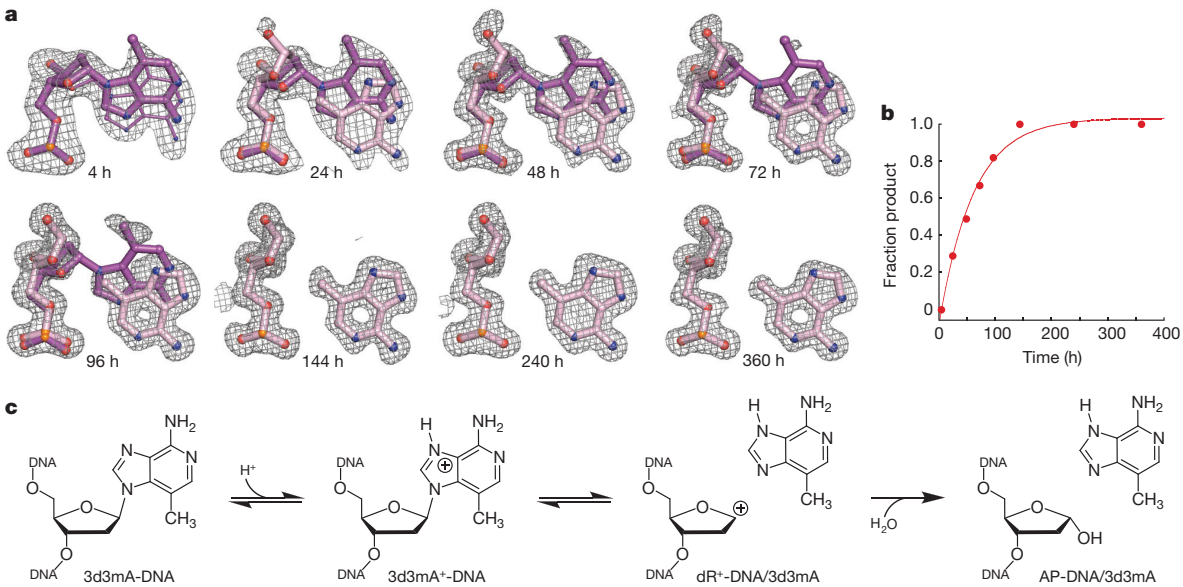

Figure 2 | Crystallographic snapshots of 3d3mA excision by AlkD. **a**, Enzymatic conversion of 3d3mA-DNA substrate (purple) to AP-DNA product and 3d3mA nucleobase (pink). The excised 3d3mA nucleobase is rotated by 180° relative to its position in the non-hydrolysed substrate. Annealed omit electron density is contoured to 2.5σ. **b**, Time course of 3d3mA excision determined from fractional occupancies of substrate and product in the crystal structures. **c**, Proposed reaction scheme showing protonation and excision of 3d3mA.

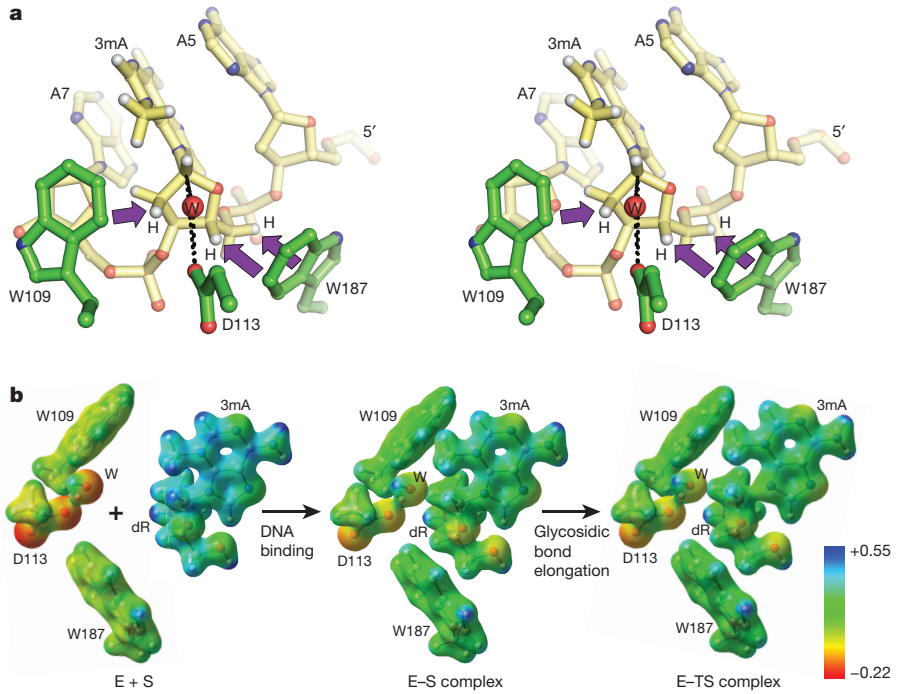

Figure 3 | 3mA recognition and excision through charge–dipole and CH–π interactions. a, Simulated AlkD–3mA-DNA complex (stereo image). Charge–dipole and hydrogen-bonding interactions are depicted as black dashed lines. CH–π interactions are shown as purple arrows. **b**, Electrostatic potential surfaces of catalytic residues and 3mA nucleoside before protein–DNA binding (E + S), in the enzyme–substrate (E–S) complex and in an approximate enzyme–transition state (E–TS) complex. All structures were determined computationally. Potentials were scaled to −0.22–0.55 atomic units on an isodensity surface of 0.05 electrons bohr^{-3}.

complexes crystallized at pH 7.0 (Extended Data Fig. 3 and Extended Data Table 3). We also did not observe cleavage in crystals grown at pH 5.7 in which AlkD bound 3d3mA-DNA in a non-catalytic orientation that placed the lesion on the opposite face of the duplex and away from the protein[16] (Extended Data Fig. 4). Thus, the AlkD–3d3mA-DNA structure presented here represents a bona fide enzyme–substrate complex that enabled visualization of the endpoints of the glycosylase reaction.

We probed the intervening step of the reaction trajectory by determining a structure representing the oxocarbenium intermediate, using DNA containing 1′-aza-2′,4′-dideoxyribose (1aR) and 3mA nucleobase (Fig. 1b and Extended Data Table 3). Relative to the position of the 3d3mA nucleotide, the cationic 1aR moiety is shifted slightly towards the surface of AlkD, which enhances electrostatic interactions with Asp113 and the nucleophilic water (Fig. 1e). These same interactions would stabilize the high-energy oxocarbenium intermediate formed upon cleavage of the glycosidic bond. A nearly identical arrangement is present in the product-like complex containing tetrahydrofuran (THF)-DNA and 3mA nucleobase (Fig. 1b, f and Extended Data Table 3). The only notable exception is a small rotation of the neutral THF ring away from Asp113. In both ternary complexes, the 3mA nucleobase is retained in the DNA duplex and paired with the complementary thymine, maintaining stacking interactions with the flanking bases (Fig. 1e, f). While base stacking is altered upon shearing of the 3d3mA•T base pair, it is never fully disrupted and is completely restored following cleavage of the *N*-glycosidic bond. In stark contrast to the traditional base-flipping mechanism, there is no evidence from these structures that a void in the duplex is created at any point along the reaction trajectory that would require stabilization by a DNA intercalating residue. Furthermore, these structures indicate that after shearing of the 3d3mA•T base pair, minimal movement of the protein and the DNA is necessary for either bond cleavage or nucleophile addition to occur.

The manner in which Trp109 and Trp187 contribute to binding and catalysis[17,18] has so far been unknown. The new AlkD–DNA structures reveal that both residues form CH–π interactions[20] with C2′, C4′ and C5′ of the 3d3mA nucleotide (Fig. 3a). To gain insight into how these weakly polar contacts contribute to recognition and excision of 3mA, we used a reductive computational approach with only the three catalytic residues, the nucleophilic water and the lesion. Electrostatic potential calculations showed that substantial cationic character is present on both the 3mA nucleobase and the deoxyribose (Fig. 3b and Extended Data Fig. 5). Importantly, increased positive charge on the deoxyribose correlated with stronger calculated binding energies, suggesting a means by which AlkD might recognize cationic alkylpurine lesions through backbone contacts (Extended Data Fig. 5). This would enhance detection of altered base pairing or base stacking[21] without the need to interact with the modified nucleobase directly. The electrostatic potential calculations also revealed that additional positive charge is transferred to the deoxyribose upon elongation of the *N*-glycosidic bond (Extended Data Fig. 5). Correspondingly, preferential binding and stabilization of this transition-state-like structure resulted in a theoretical 10^3–10^4-fold rate enhancement of glycosidic bond cleavage. Roughly half of this enhancement was attributed to the increasingly polar CH–π interactions provided by Trp109 and Trp187 (Extended Data Fig. 5). While interactions of this type are widespread among proteins and are prevalent in protein–DNA complexes[22,23], to our knowledge, this is the first indication that CH–π interactions might function in a catalytic capacity in DNA repair. These interactions are reminiscent of the π–π and cation–π interactions used by base-flipping enzymes to recognize extrahelical nucleobases[24,25], but are distinctly different in their involvement of the deoxyribose, and may be fundamental to lesion excision in the absence of base flipping.

The unique mechanism reported here explains our previous finding that AlkD, but not human AAG, removes bulky, cationic pyridyloxobutyl adducts[16]. While extrahelical pyridyloxobutyl adducts are accommodated by the large nucleobase binding pockets of alkyltransferase-like proteins[26], the relatively small active site pockets of AAG and other base-flipping DNA glycosylases impose tighter steric limitations. AlkD, however, does not rely on a base-flipping mechanism

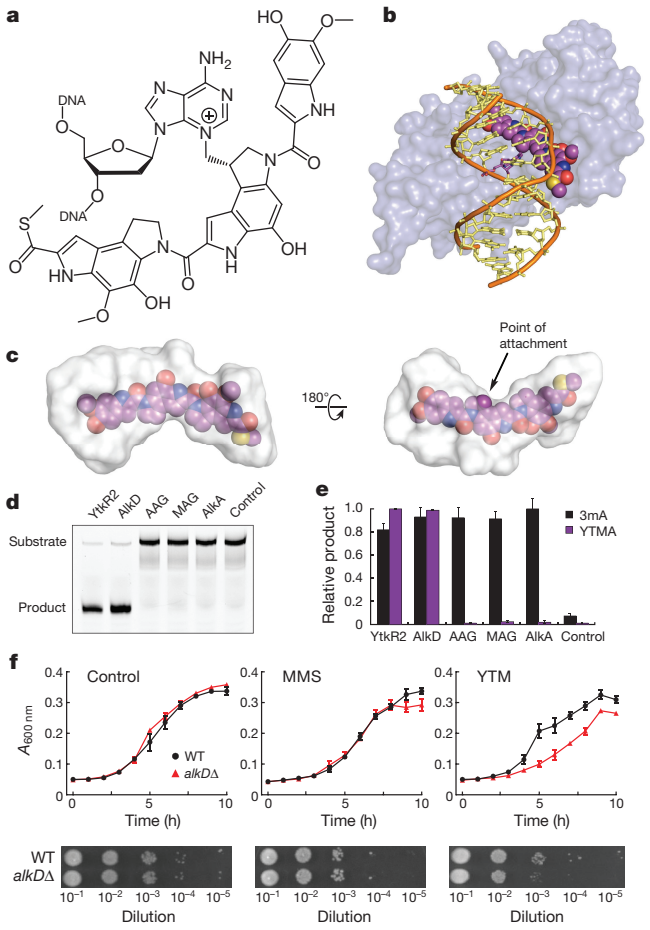

Figure 4 | Excision of *N*3-yatakemycyladenine by AlkD. a, YTMA. **b**, Modelled AlkD–YTMA-DNA complex. **c**, Solvent-filled cavity between AlkD and 3d3mA-DNA into which YTM was modelled. **d**, *In vitro* YTMA excision monitored by separation of full-length YTMA-DNA substrate from cleaved AP-DNA product by denaturing gel electrophoresis. **e**, Quantification of *in vitro* excision of 3mA (black) and YTMA (purple) by diverse alkylpurine DNA glycosylases. Error bars denote s.d. from three replicate experiments. **f**, Growth of wild-type (black) and *alkD*-knockout (red) strains of *B. anthracis* in the presence of no drug (control), 2 mM MMS and 10 nM YTM. Error bars denote s.e.m. from three replicate experiments.

and therefore is not restricted in this fashion, suggesting it may have a cellular role in the repair of bulky lesions. Specificity for bulky alkyl adducts would explain the coexistence of several alkylpurine glycosylases in numerous bacterial species[14]. Consistent with this notion, an AlkD orthologue from *Streptomyces* sp. TP-A0356 has been found to excise 815-dalton (Da) *N*3-yatakemycyladenine (YTMA) adducts from DNA[27] (Fig. 4a). Yatakemycin (YTM) is a minor-groove DNA-alkylating agent belonging to the duocarmycin family of antibiotic and antitumour drugs[6]. The gene cluster responsible for biosynthesis of YTM encodes the DNA glycosylase YtkR2, which confers resistance to YTM by excising YTMA lesions[27].

On the basis of the sequence similarity between YtkR2 and AlkD, we proposed that AlkD would also have activity for YTMA. There is an extended solvent-filled volume between the protein and the minor groove in the AlkD–3d3mA-DNA complex that can accommodate YTM modelled onto the *C*3 position of 3d3mA without introducing steric clashes or disrupting catalytic interactions (Fig. 4b, c). Using a standard *in vitro* DNA glycosylase assay, we found that AlkD excised YTMA from DNA with the same efficiency as YtkR2 (Fig. 4d, e). By contrast, the alkylpurine DNA glycosylases AAG, MAG and AlkA failed to excise YTMA but readily removed 3mA (Fig. 4d, e). To determine the specificity of AlkD for YTMA in cells, we constructed a *Bacillus anthracis* strain lacking *alkD* and tested its sensitivity against YTM and methyl methanesulfonate (MMS). MMS primarily produces 3mA and *N*7-methylguanine adducts that are removed by canonical alkylpurine DNA glycosylases[5]. In the absence of alkylating agent, deletion of *alkD* had no effect on the growth of *B. anthracis* (Fig. 4f and Extended Data Fig. 6). Similarly, *alkD* cells were no more sensitive to MMS than wild-type cells (Fig. 4f and Extended Data Fig. 6), most likely as a result of activity from the other alkylpurine glycosylases (AAG, AlkA and AlkC) still present in the deletion strain. Conversely, deletion of *alkD* caused a marked increase in sensitivity to YTM, consistent with AlkD-catalysed excision of YTMA *in vivo* (Fig. 4f and Extended Data Fig. 6). This suggests that the primary role of AlkD in the cell is to repair larger alkyl adducts such as YTMA that are not normally corrected by the base excision repair pathway.

This work establishes that, contrary to dogma, substrate recognition and catalysis by DNA glycosylases can occur in the absence of base flipping. There is evidence that other enzymes are able to detect DNA damage and even discriminate between different chemical modifications before flipping[28–30]. That AlkD is limited to removing inherently labile cationic lesions strongly suggests that the main function of the nucleobase binding pocket in canonical DNA glycosylases is to increase the leaving-group potential of the nucleobase substrate, as opposed to merely discriminating against non-substrate nucleobases. With this capability, however, comes a limit on the size of the adduct that can be excised. Ultimately, the greatest benefit of a non-base-flipping mechanism may be the ability to repair bulky lesions.

Online Content Methods, along with any additional Extended Data display items and Source Data, are available in the online version of the paper; references unique to these sections appear only in the online paper.

Received 22 July; accepted 18 September 2015.
Published online 28 October 2015.

1. Fromme, J. C. & Verdine, G. L. Base excision repair. *Adv. Protein Chem.* **69,** 1–41 (2004).
2. Hitomi, K., Iwai, S. & Tainer, J. A. The intricate structural chemistry of base excision repair machinery: implications for DNA damage recognition, removal, and repair. *DNA Repair (Amst.)* **6,** 410–428 (2007).
3. Slupphaug, G. *et al.* A nucleotide-flipping mechanism from the structure of human uracil-DNA glycosylase bound to DNA. *Nature* **384,** 87–92 (1996).
4. Stivers, J. T. Site-specific DNA damage recognition by enzyme-induced base flipping. *Prog. Nucleic Acid Res. Mol. Biol.* **77,** 37–65 (2004).
5. Brooks, S. C., Adhikary, S., Rubinson, E. H. & Eichman, B. F. Recent advances in the structural mechanisms of DNA glycosylases. *Biochim. Biophys. Acta* **1834,** 247–271 (2013).
6. Igarashi, Y. *et al.* Yatakemycin, a novel antifungal antibiotic produced by *Streptomyces* sp. TP-A0356. *J. Antibiot. (Tokyo)* **56,** 107–113 (2003).
7. Alberts, S. R., Suman, V. J., Pitot, H. C., Camoriano, J. K. & Rubin, J. Use of KW-2189, a DNA minor groove-binding agent, in patients with hepatocellular carcinoma: a north central cancer treatment group (NCCTG) phase II clinical trial. *J. Gastrointest. Cancer* **38,** 10–14 (2007).
8. Friedberg, E. C. *et al. DNA Repair and Mutagenesis* 2nd edn (ASM Press, 2006).
9. Larson, K., Sahm, J., Shenkar, R. & Strauss, B. Methylation-induced blocks to *in vitro* DNA replication. *Mutat. Res.* **150,** 77–84 (1985).
10. Plosky, B. S. *et al.* Eukaryotic Y-family polymerases bypass a 3-methyl-2′-deoxyadenosine analog *in vitro* and methyl methanesulfonate-induced DNA damage *in vivo*. *Nucleic Acids Res.* **36,** 2152–2162 (2008).
11. Drohat, A. C. & Maiti, A. Mechanisms for enzymatic cleavage of the N-glycosidic bond in DNA. *Org. Biomol. Chem.* **12,** 8367–8378 (2014).
12. Stivers, J. T. & Jiang, Y. L. A mechanistic perspective on the chemistry of DNA repair glycosylases. *Chem. Rev.* **103,** 2729–2760 (2003).
13. Hendershot, J. M. & O'Brien, P. J. Critical role of DNA intercalation in enzyme-catalyzed nucleotide flipping. *Nucleic Acids Res.* **42,** 12681–12690 (2014).
14. Alseth, I. *et al.* A new protein superfamily includes two novel 3-methyladenine DNA glycosylases from *Bacillus cereus*, AlkC and AlkD. *Mol. Microbiol.* **59,** 1602–1609 (2006).
15. Rubinson, E. H., Metz, A. H., O'Quin, J. & Eichman, B. F. A new protein architecture for processing alkylation damaged DNA: the crystal structure of DNA glycosylase AlkD. *J. Mol. Biol.* **381,** 13–23 (2008).
16. Rubinson, E. H., Gowda, A. S., Spratt, T. E., Gold, B. & Eichman, B. F. An unprecedented nucleic acid capture mechanism for excision of DNA damage. *Nature* **468,** 406–411 (2010).
17. Dalhus, B. *et al.* Structural insight into repair of alkylated DNA by a new superfamily of DNA glycosylases comprising HEAT-like repeats. *Nucleic Acids Res.* **35,** 2451–2459 (2007).
18. Mullins, E. A., Rubinson, E. H. & Eichman, B. F. The substrate binding interface of alkylpurine DNA glycosylase AlkD. *DNA Repair (Amst.)* **13,** 50–54 (2014).

19. Mullins, E. A. *et al.* An HPLC-tandem mass spectrometry method for simultaneous detection of alkylated base excision repair products. *Methods* **64,** 59–66 (2013).
20. Plevin, M. J., Bryce, D. L. & Boisbouvier, J. Direct detection of CH/π interactions in proteins. *Nature Chem.* **2,** 466–471 (2010).
21. Yang, W. Poor base stacking at DNA lesions may initiate recognition by many repair proteins. *DNA Repair (Amst.)* **5,** 654–666 (2006).
22. Brandl, M., Weiss, M. S., Jabs, A., Suhnel, J. & Hilgenfeld, R. C-H···π-interactions in proteins. *J. Mol. Biol.* **307,** 357–377 (2001).
23. Wilson, K. A., Kellie, J. L. & Wetmore, S. D. DNA-protein π-interactions in nature: abundance, structure, composition and strength of contacts between aromatic amino acids and DNA nucleobases or deoxyribose sugar. *Nucleic Acids Res.* **42,** 6726–6741 (2014).
24. Metz, A. H., Hollis, T. & Eichman, B. F. DNA damage recognition and repair by 3-methyladenine DNA glycosylase I (TAG). *EMBO J.* **26,** 2411–2420 (2007).
25. Wilkinson, O. J. *et al.* Alkyltransferase-like protein (Atl1) distinguishes alkylated guanines for DNA repair using cation-π interactions. *Proc. Natl Acad. Sci. USA* **109,** 18755–18760 (2012).
26. Tubbs, J. L. *et al.* Flipping of alkylated DNA damage bridges base and nucleotide excision repair. *Nature* **459,** 808–813 (2009).
27. Xu, H. *et al.* Self-resistance to an antitumor antibiotic: a DNA glycosylase triggers the base-excision repair system in yatakemycin biosynthesis. *Angew. Chem. Int. Ed. Engl.* **51,** 10532–10536 (2012).
28. Qi, Y. *et al.* Encounter and extrusion of an intrahelical lesion by a DNA repair enzyme. *Nature* **462,** 762–766 (2009).
29. Imamura, K., Averill, A., Wallace, S. S. & Doublie, S. Structural characterization of viral ortholog of human DNA glycosylase NEIL1 bound to thymine glycol or 5-hydroxyuracil-containing DNA. *J. Biol. Chem.* **287,** 4288–4298 (2012).
30. Adhikary, S. & Eichman, B. F. Analysis of substrate specificity of *Schizosaccharomyces pombe* Mag1 alkylpurine DNA glycosylase. *EMBO Rep.* **12,** 1286–1292 (2011).

Supplementary Information is available in the online version of the paper.

Acknowledgements We thank C. Rizzo and T. Johnson Salyard for assistance with oligodeoxynucleotide synthesis and E. Skaar and L. Mike for assistance with genetic manipulation of *B. anthracis*. This work was funded by the National Science Foundation (MCB-1122098 and MCB-1517695 to B.F.E.) and the National Institutes of Health (R01ES019625 to B.F.E. and R01CA067985 to S.S.D.). Support for the Vanderbilt Robotic Crystallization Facility was also provided by the National Institutes of Health (S10RR026915). Use of the Advanced Photon Source, an Office of Science User Facility operated for the US Department of Energy Office of Science by Argonne National Laboratory, was supported by the US Department of Energy (DE-AC02-06CH11357). Use of LS-CAT Sector 21 was supported by the Michigan Economic Development Corporation and the Michigan Technology Tri-Corridor (085P1000817). E.A.M. and Z.D.P. were partially supported by the Vanderbilt Training Program in Environmental Toxicology (T32ES07028).

Author Contributions E.A.M. and B.F.E. conceived the project; E.A.M., R.S., Z.D.P. and B.F.E. designed experiments; E.A.M. performed biochemical and structural experiments; R.S. performed cellular experiments; Z.D.P. performed computational experiments; P.K.Y., S.S.D. and Y.I. supplied reagents; E.A.M., R.S., Z.D.P. and B.F.E. analysed data and wrote the paper; all authors commented on the manuscript.

Author Information Atomic coordinates and structure factors have been deposited in the Protein Data Bank under accession codes 5CL3, 5CL4, 5CL5, 5CL6, 5CL7, 5CL8, 5CL9, 5CLA, 5CLB, 5CLC, 5CLD and 5CLE. Reprints and permissions information is available at www.nature.com/reprints. The authors declare no competing financial interests. Readers are welcome to comment on the online version of the paper. Correspondence and requests for materials should be addressed to B.F.E. (brandt.eichman@vanderbilt.edu).

METHODS

Oligodeoxynucleotide synthesis. 3d3mA phosphoramidite was purchased from Berry and Associates. 1aR phosphoramidite was synthesized with minor modification of a previously described method[31]. Both were incorporated into oligodeoxynucleotides using standard solid-phase techniques. The resulting products were purified by reverse-phase HPLC and verified by mass spectrometry. All other oligodeoxynucleotides were purchased from Integrated DNA Technologies and used without further purification.

Protein purification. Human (Δ79)AAG[32], *Saccharomyces cerevisiae* MAG[30], *Escherichia coli* AlkA[33] and *B. cereus* AlkD[15] were purified as previously described. The gene encoding YtkR2 (GenBank accession IADZ13541) was synthesized by DNA2.0 and ligated into a modified pET27 expression vector encoding a Rhinovirus 3C cleavable hexahistidine tag. YtkR2 overproduction in *E. coli* HMS174(DE3) cells was induced at 16 °C after addition of 0.5 mM isopropyl β-D-1-thiogalactopyranoside (IPTG). Cells were collected from LB medium by centrifugation, resuspended in buffer L (50 mM Tris-HCl, pH 7.5, 500 mM NaCl and 20% (v/v) glycerol) and lysed on ice by gentle sonication. Cleared lysate was applied to a Ni-NTA column equilibrated in buffer L. The column was then washed with buffer L containing 2 mM histidine and eluted with buffer L containing 100 mM EDTA. Pooled fractions were supplemented with 2 mM dithiothreitol (DTT) before overnight cleavage of the affinity tag. Cleaved YtkR2 was diluted tenfold in buffer H (50 mM Tris-HCl, pH 7.5, 20% (v/v) glycerol, 2 mM DTT and 0.1 mM EDTA) before being applied to a heparin Sepharose column equilibrated in buffer H. The column was then washed with buffer H containing 50 mM NaCl and eluted by linearly increasing to buffer H containing 1 M NaCl. Pooled fractions were passed through a Ni-NTA column equilibrated in buffer L to remove trace protein contaminants. The column was subsequently rinsed with buffer L containing 2 mM histidine to elute weakly bound YtkR2. The flow-through and the rinse were then combined, concentrated by ultracentrifugation and applied to a Superdex 200 column equilibrated in buffer S (20 mM Bis-tris propane, pH 6.5, 400 mM NaCl, 20% (v/v) glycerol, 2 mM DTT and 0.1 mM EDTA). YtkR2 was eluted with additional buffer S, concentrated to 3 mg ml^{-1} by ultracentrifugation, flash-frozen in liquid nitrogen and stored at −80 °C.

Crystallization of AlkD–DNA. DNA annealing reactions contained 0.54 mM 9-mer A [d(AAGCAXACC)/d(TGGTTTGCT)], 9-mer B [d(AAGCCXCCC)/d(TGGGTGGCT)], or 12-mer [d(CCCGAXAGTCCG)/d(CGGACTTTCGGG)] oligodeoxynucleotides, 10 mM MES, pH 6.5, and 40 mM NaCl. Reactions containing 1aR•T-DNA or THF•T-DNA were supplemented with 27 mM 3mA nucleobase. Strands were annealed by heating to 85 °C and slowly cooling to 20 °C over several hours. AlkD–DNA complexes were formed by mixing 0.45 mM protein and 0.54 mM DNA solutions in equal volumes and incubating at 4 °C for 30 min. Complexes containing 9-mer DNA were crystallized using the sitting drop vapour diffusion method. Drops were prepared from 2 μl of protein–DNA solution (0.22 mM AlkD and 0.27 mM DNA), 2 μl of reservoir solution (22–25% (w/v) PEG 8,000, 50 mM HEPES, pH 7.0, and 50 mM $CaCl_2$), and 1 μl of additive solution (5% (w/v) benzamidine hydrochloride) and equilibrated against an additional 500 μl of reservoir solution at 21 °C. Crystals were collected after 24 h, briefly soaked in reservoir solution supplemented with 15% (v/v) glycerol and flash-cooled in liquid nitrogen. Complexes containing 12-mer DNA were crystallized using the hanging drop vapour diffusion technique. Drops were assembled from 2 μl of protein–DNA solution (0.22 mM AlkD and 0.27 mM DNA), 2 μl of reservoir solution (15–19% (w/v) PEG 4,000, 42 mM sodium acetate, pH 4.6, 85 mM ammonium acetate and 5% (v/v) glycerol) and 1 μl of seed solution (submicroscopic crystals of AlkD–1mA•T-DNA) and equilibrated against an additional 500 μl of reservoir solution at 21 °C. Crystals were collected after 4–360 h, briefly soaked in reservoir solution supplemented with 15% (v/v) glycerol and flash-cooled in liquid nitrogen.

X-ray data collection and structure refinement. X-ray diffraction data were collected at beamlines 21-ID-F and 21-ID-G at the Advanced Photon Source and processed using HKL2000 (ref. 34). Data collection statistics are provided in Extended Data Tables 1–3. A previously determined model of AlkD (PDB accession 3BVS) was positioned with Phaser[35], while DNA was manually built in Coot[36], guided by inspection of $2mF_o - DF_c$ and $mF_o - DF_c$ electron density maps. The entirety of the 12-mer oligodeoxynucleotide duplex was readily apparent, as were AlkD residues 1–229 and two non-native residues (−1–0) from the cleaved N-terminal affinity tag, but not the last eight residues (230–237) at the C terminus. As with the 12-mer, the complete 9-mer duplexes were visible in the density maps. However, three residues (52–54) between helix C and helix D and twelve residues (226–237) at the C terminus could not be reliably modelled. Atomic coordinates, temperature factors and fractional occupancies were refined in PHENIX[37]. The final AlkD–DNA models were validated using MolProbity[38] and contained no residues in the disallowed regions of the Ramachandran plot. Refinement and validation statistics are given in Extended Data Tables 1–3.

All structure images were created in PyMOL (https://www.pymol.org). $mF_o - DF_c$ omit electron density maps were calculated using PHENIX by removing the lesion and the opposing thymine and then performing simulated annealing on the remaining AlkD–DNA complex to minimize model bias. Maps were carved around the omitted atoms with a 1.5–2.0 Å radius and contoured to 2.5σ. YTM was manually docked in the AlkD–3d3mA-DNA complex after defining the cavity between the protein and the DNA with Hollow[39]. Simulated structures shown in Fig. 3a and Extended Data Fig. 1c were generated from AlkD–3d3mA-DNA crystal structures by manually removing or transmuting atoms and without performing subsequent computational optimization.

Preparation of YTMA-DNA. YTM was purified from *Streptomyces* sp. TP-A0356 culture as previously described[6]. Adduction reactions containing 150 μM YTM, 10 μM fluorescein (FAM)-labelled DNA (FAM-d(CGGGCGGCGGCAAAGGGCGCGGGCC)/d(GGCCCGCGCCCTTTGCCGCCGCCCG); underline denotes nucleotide modified by YTM), 10 mM MES, pH 6.5, 40 mM NaCl and 10% (v/v) DMSO were incubated at 25 °C for 24 h and periodically mixed by inversion. YTM-modified DNA was then separated from free YTM by passage through a G25 size exclusion column equilibrated in 10 mM MES, pH 6.5, and 40 mM NaCl and stored at −80 °C.

Quantification of base excision. Reaction mixtures containing 5 μM enzyme, 10 μg of methylated calf thymus DNA or 100 nM YTM-modified oligodeoxynucleotide duplex, 50 mM Bis-tris propane, pH 6.5, 100 mM NaCl, 5% (v/v) glycerol, 2 mM DTT, 0.1 mM EDTA and 0.1 mg ml^{-1} BSA were incubated at 25 °C for 6 h. Excision of 3mA was quantified by measuring cleaved nucleobase using a previously described HPLC–MS/MS method[19]. Excision of YTMA was quantitated by separating the 25-mer substrate from the 12-mer product using standard electrophoretic techniques[19]. Strand breakage of 25-mer abasic oligodeoxynucleotide was induced by heating the reaction mixture at 70 °C for 30 min in the presence of 0.2 M NaOH.

Preparation of *alkD*Δ cells. The 1-kilobase flanking regions surrounding *alkD* were inserted into the knockout-plasmid pLM4 using standard molecular biology techniques[40]. The modified plasmid was propagated in *E. coli* K1077 before introduction by electroporation into *B. anthracis* Sterne cells[41,42]. *B. anthracis* colonies containing the plasmid were grown on LB plates supplemented with 20 μg ml^{-1} kanamycin at 42.5 °C for 1–2 days to generate merodiploids with plasmid DNA integrated into their chromosomal DNA. Merodiploids were then grown in LB medium for 1 day at 30 °C to facilitate elimination of redundant DNA from their genomes. Cultures were serially diluted and grown on LB plates without kanamycin for 1 day at 30 °C so that colonies lacking *alkD* could be identified by PCR screening.

Determination of YTM and MMS resistance. Overnight cultures of *B. anthracis* Sterne (wild-type and *alkD*Δ) grown at 30 °C were diluted 1:100 in 100 μl of LB medium in the presence or absence of 2–40 nM YTM or 1–10 mM MMS in a 96-well flat-bottom plate. The plate was incubated at 30 °C with shaking for 20 h, and cell density was measured at 600 nm every hour using a Synergy 2 multi-detector microplate reader. Before each measurement, the plate was gently vortexed to ensure full resuspension of sedimented cells. Experiments were performed in triplicate.

Overnight cultures of *B. anthracis* Sterne (wild-type and *alkD*Δ) grown at 30 °C were diluted 1:100 in 5 ml of LB medium and incubated at 30 °C with shaking until early logarithmic phase. Culture aliquots (5 μl) were then tenfold serially diluted ($1:10^{-1}$–$1:10^{-5}$) and spotted on LB plates prepared with or without 2–40 nM YTM or 1–10 mM MMS. Plates were incubated at 37 °C and imaged after 2 days. Experiments were performed in duplicate.

Calculation overview. All calculations were performed using Gaussian 09 (http://www.gaussian.com/g_prod/g09.htm). Atomic coordinates for computationally optimized structures are provided in Supplementary Data 1.

pK_a calculation. The aqueous pK_a microacidity constant of *N*7-protonated 3-deaza-3,9-dimethyladenine (3d3m9mA) was calculated using the isodesmic reaction method[43] with *N*7-protonated 9-methyladenine (9mA) used as the reference acid (aqueous $pK_a = 2.96$)[44]. Neutral and *N*7-protonated 9mA and 3d3m9mA were optimized to minima using Truhlar's M06-2X density functional[45] with the split-valence 6–311+G(2d,p) basis set and the SMD solvation model[46]. Optimized structures were confirmed minima by vibrational frequency analyses. Single point evaluations were carried out on the optimized structures in the presence of implicit solvent (water) at the M06-2X/aug-cc-pVTZ level. Thermal corrections to Gibbs free energies were taken from the frequency calculations and applied to electronic energies determined at the M06-2X/aug-cc-pVTZ level. Proton exchange energetics (ΔG_{exchg}) between 9mA and 3d3m9mA were then determined using the corrected electronic energies.

Constrained optimization of AlkD–lesion structures. The crystal structure of AlkD bound to 3d3mA-DNA served as the starting point for all computational structural optimizations. Atomic coordinates were extracted for AlkD residues

Trp109, Asp113 and Trp187 as well as HOH308 and 3d3mA. Hydrogen atoms were added manually to satisfy all valences, and Asp113 was assumed to be in carboxylate form. To reduce computational cost during structural optimizations and subsequent calculations, protein residues were truncated to their respective side chains (β-carbons as methyl groups), and 3d3mA was truncated to the corresponding 2′-deoxynucleoside. The starting point for the structure of 3mA was generated by replacing carbon with nitrogen at the 3-position of the purine ring in 3d3mA. The starting point for the transition state approximation (TSA) was generated by elongating the glycosidic bond of optimized 3mA by 0.5 Å. This distance was chosen based on the computationally determined transition state for excision of uracil by UDG[47]. Finally, the starting point for dR^+ was generated by deleting the 3d3mA nucleobase from the corresponding 2′-deoxynucleoside, leaving an open valence on C1′.

Structural optimizations were performed in the gas phase using the M06-2X functional in conjunction with the 6–31+G(d) basis set. In all cases, the Cartesian coordinates for all non-hydrogen atoms in AlkD residues Trp109, Asp113 and Trp187 as well as HOH308 were frozen using the freeze code −1 in the molecular coordinates specification. Additionally, the 3′- and 5′-oxygen atoms of all 2′-deoxynucleosides were frozen to simulate the experimentally observed lack of motion in the phosphodiester backbone in the full AlkD–DNA complexes. All other atoms, with the exception of C1′ and N9 in the TSA, were allowed to move during optimizations. Stationary points derived from geometry optimizations on these reduced-dimension potential energy surfaces were verified as minima by vibrational frequency analyses. Frequency analyses were performed at the same level of theory and on the same reduced-dimension surfaces as the geometry optimizations. Using this approach, freezing Cartesian coordinates results in zeroing of elements in the Hessian associated with the frozen atoms. As such, the expected imaginary frequency resulting from elongation of the glycosidic bond in the TSA was not observed. All structures, including the TSA, afforded zero imaginary frequencies.

Calculation of binding energy and catalytic rate enhancement. Binding energies of the truncated AlkD residues and the catalytic water to 3d3mA, 3mA, TSA and dR^+ were determined using the M06-2X functional. Structural optimizations were carried out as described above using the 6–31+G(d) basis set, and single point evaluations were carried out using the 6–311++G(3df,2p) basis set. The basis set superposition error was accounted for using the counterpoise method[48], in which AlkD residues and the catalytic water were defined as the first fragment and the 2′-deoxynucleosides were defined as the second fragment. Because heavy atoms in AlkD residues were frozen at their experimentally determined atomic positions, binding energies were evaluated as differences in zero point-uncorrected electronic energies. This approach reproduced experimental gas-phase binding energies to within 1 kcal mol^{-1} for two prototypical CH–π systems, including neutral CH_4/benzene (experimental 1.03–1.13 kcal mol^{-1} versus calculated 1.6 kcal mol^{-1})[49] and cationic $(CH_3)_4N^+$/benzene (experimental 9.4 kcal mol^{-1} versus calculated 10.3 kcal mol^{-1})[50]. To determine the individual contributions of Trp109, Asp113, Trp187 and HOH308 to ensemble binding energies, the counterpoise method was again employed as described above, but with the atoms in Trp109, Asp113, Trp187 or HOH308 replaced with the corresponding Gaussian ghost atoms. The contribution of each residue to the total binding energy (defined as $BE_{individual(x)} = BE_{ensemble} - BE_{ensemble,ghost(x)}$) was computed as the difference between the ensemble binding energy and that where Trp109, Asp113, Trp187 or HOH308 had been replaced with ghost atoms. Complexes containing ghost atoms were not reoptimized, which may affect individual binding energies. However, using this method, between 92% and 99% of the ensemble binding energy was accounted for in each complex.

The barrier to bond elongation (defined as $\Delta E = E_{TSA} - E_{3mA}$) was calculated in the presence ($\Delta E = 18.1$ kcal mol^{-1}) and absence ($\Delta E = 23.0$ kcal mol^{-1}) of Trp109, Asp113, Trp187 and HOH308. The difference in these values ($\Delta\Delta E = 4.9$ kcal mol^{-1}) was taken as the catalytic contribution of AlkD to 3mA excision. This process was repeated for complexes in which atoms in each residue or the catalytic water had been replaced with ghost atoms. For each series, $\Delta\Delta E$ values were computed as outlined above, and the difference between each of these $\Delta\Delta E$ values and that of the full ensemble was taken as the individual contribution of the omitted residue to catalysis. Estimated rate enhancements were calculated from these values by substituting $\Delta\Delta E$ for $\Delta\Delta G^{\ddagger}$ in the Eyring equation at 25 °C. The barrier to bond elongation ($\Delta E = 23.0$ kcal mol^{-1}) calculated with this approach is consistent with the activation enthalpy for depurination of 3mA ($\Delta H^{\ddagger} = 23.5$ kcal mol^{-1}) extrapolated from empirically determined half-lives[51].

Quantitation of charge transfer and generation of electrostatic potential maps. Charge transfer from AlkD residues Trp109, Asp113 and Trp187 and HOH308 to the lesions was quantitated by performing Merz–Singh–Kollman (MK) population analyses[52,53] on each complex and on each individual component (either AlkD and the catalytic water or the lesion). To correct for potential basis set superposition error in population analyses, the appropriate Gaussian ghost atoms were used to maintain consistent basis between fragments and complexes. Partial atomic charges derived from MK population analyses were summed for all atoms in AlkD and for the lesion, affording the corresponding group charges. The arithmetic difference between group charges in the AlkD–lesion complex and AlkD or the lesion alone were taken as the amount of charge transferred upon complex formation and expressed as percentages. Electrostatic potential maps were generated from densities computed at the M06-2X/6–311++G(3df,2p) level with ghost atoms omitted for visual clarity. Potentials were scaled to −0.22–0.55 atomic units on an isodensity surface of 0.05 electrons bohr^{-3}.

31. Chu, A. M., Fettinger, J. C. & David, S. S. Profiling base excision repair glycosylases with synthesized transition state analogs. *Bioorg. Med. Chem. Lett.* **21,** 4969–4972 (2011).
32. O'Brien, P. J. & Ellenberger, T. Human alkyladenine DNA glycosylase uses acid-base catalysis for selective excision of damaged purines. *Biochemistry* **42,** 12418–12429 (2003).
33. Bjelland, S., Birkeland, N. K., Benneche, T., Volden, G. & Seeberg, E. DNA glycosylase activities for thymine residues oxidized in the methyl group are functions of the AlkA enzyme in *Escherichia coli*. *J. Biol. Chem.* **269,** 30489–30495 (1994).
34. Otwinowski, Z. & Minor, W. Processing of X-ray diffraction data. *Methods Enzymol.* **276,** 307–326 (1997).
35. McCoy, A. J. *et al.* Phaser crystallographic software. *J. Appl. Crystallogr.* **40,** 658–674 (2007).
36. Emsley, P., Lohkamp, B., Scott, W. & Cowtan, K. Features and development of Coot. *Acta Crystallogr. D* **66,** 486–501 (2010).
37. Adams, P. D. *et al.* PHENIX: a comprehensive Python-based system for macromolecular structure solution. *Acta Crystallogr. D* **66**, 213–221 (2010).
38. Davis, I. W. *et al.* MolProbity: all-atom contacts and structure validation for proteins and nucleic acids. *Nucleic Acids Res.* **35,** W375–W383 (2007).
39. Ho, B. K. & Gruswitz, F. HOLLOW: generating accurate representations of channel and interior surfaces in molecular structures. *BMC Struct. Biol.* **8,** 49 (2008).
40. Mike, L. A. *et al.* Two-component system cross-regulation integrates *Bacillus anthracis* response to heme and cell envelope stress. *PLoS Pathog.* **10,** e1004044 (2014).
41. Sterne, M. Avirulent anthrax vaccine. *Onderstepoort J. Vet. Sci. Anim. Ind.* **21,** 41–43 (1946).
42. Stauff, D. L. & Skaar, E. P. *Bacillus anthracis* HssRS signalling to HrtAB regulates haem resistance during infection. *Mol. Microbiol.* **72,** 763–778 (2009).
43. Ho, J. & Coote, M. L. A universal approach for continuum solvent pK_a calculations: are we there yet? *Theor. Chem. Acc.* **125,** 3–21 (2010).
44. Kapinos, L. E., Operschall, B. P., Larsen, E. & Sigel, H. Understanding the acid–base properties of adenosine: the intrinsic basicities of N1, N3 and N7. *Chemistry* **17,** 8156–8164 (2011).
45. Zhao, Y. & Truhlar, D. G. The M06 suite of density functionals for main group thermochemistry, thermochemical kinetics, noncovalent interactions, excited states, and transition elements: two new functionals and systematic testing of four M06-class functionals and 12 other functionals. *Theor. Chem. Acc.* **120,** 215–241 (2008).
46. Marenich, A. V., Cramer, C. J. & Truhlar, D. G. Universal solvation model based on solute electron density and on a continuum model of the solvent defined by the bulk dielectric constant and atomic surface tensions. *J. Phys. Chem. B* **113,** 6378–6396 (2009).
47. Dinner, A. R., Blackburn, G. M. & Karplus, M. Uracil-DNA glycosylase acts by substrate autocatalysis. *Nature* **413,** 752–755 (2001).
48. Boys, S. F. & Bernardi, F. The calculation of small molecular interactions by the differences of separate total energies. Some procedures with reduced errors. *Mol. Phys.* **19,** 553–566 (1970).
49. Shibasaki, K., Fujii, A., Mikami, N. & Tsuzuki, S. Magnitude of the CH/π interaction in the gas phase: experimental and theoretical determination of the accurate interaction energy in benzene-methane. *J. Phys. Chem. A* **110,** 4397–4404 (2006).
50. Meot-Ner, M. & Deakyne, C. A. Unconventional ionic hydrogen-bonds. 1. $CH^{\delta+}\cdots X$. Complexes of quaternary ions with n- and π-donors. *J. Am. Chem. Soc.* **107,** 469–474 (1985).
51. Osborne, M. R. & Phillips, D. H. Preparation of a methylated DNA standard, and its stability on storage. *Chem. Res. Toxicol.* **13,** 257–261 (2000).
52. Singh, U. C. & Kollman, P. A. An approach to computing electrostatic charges for molecules. *J. Comput. Chem.* **5,** 129–145 (1984).
53. Besler, B. H., Merz, K. M. & Kollman, P. A. Atomic charges derived from semiempirical methods. *J. Comput. Chem.* **11,** 431–439 (1990).
54. Ramstein, J. & Lavery, R. Energetic coupling between DNA bending and base pair opening. *Proc. Natl Acad. Sci. USA* **85,** 7231–7235 (1988).
55. Adhikary, S., Cato, M. C., McGary, K. L., Rokas, A. & Eichman, B. F. Non-productive DNA damage binding by DNA glycosylase-like protein Mag2 from *Schizosaccharomyces pombe*. *DNA Repair (Amst.)* **12,** 196–204 (2013).
56. Dalhus, B. *et al.* Sculpting of DNA at abasic sites by DNA glycosylase homolog Mag2. *Structure* **21,** 154–166 (2013).

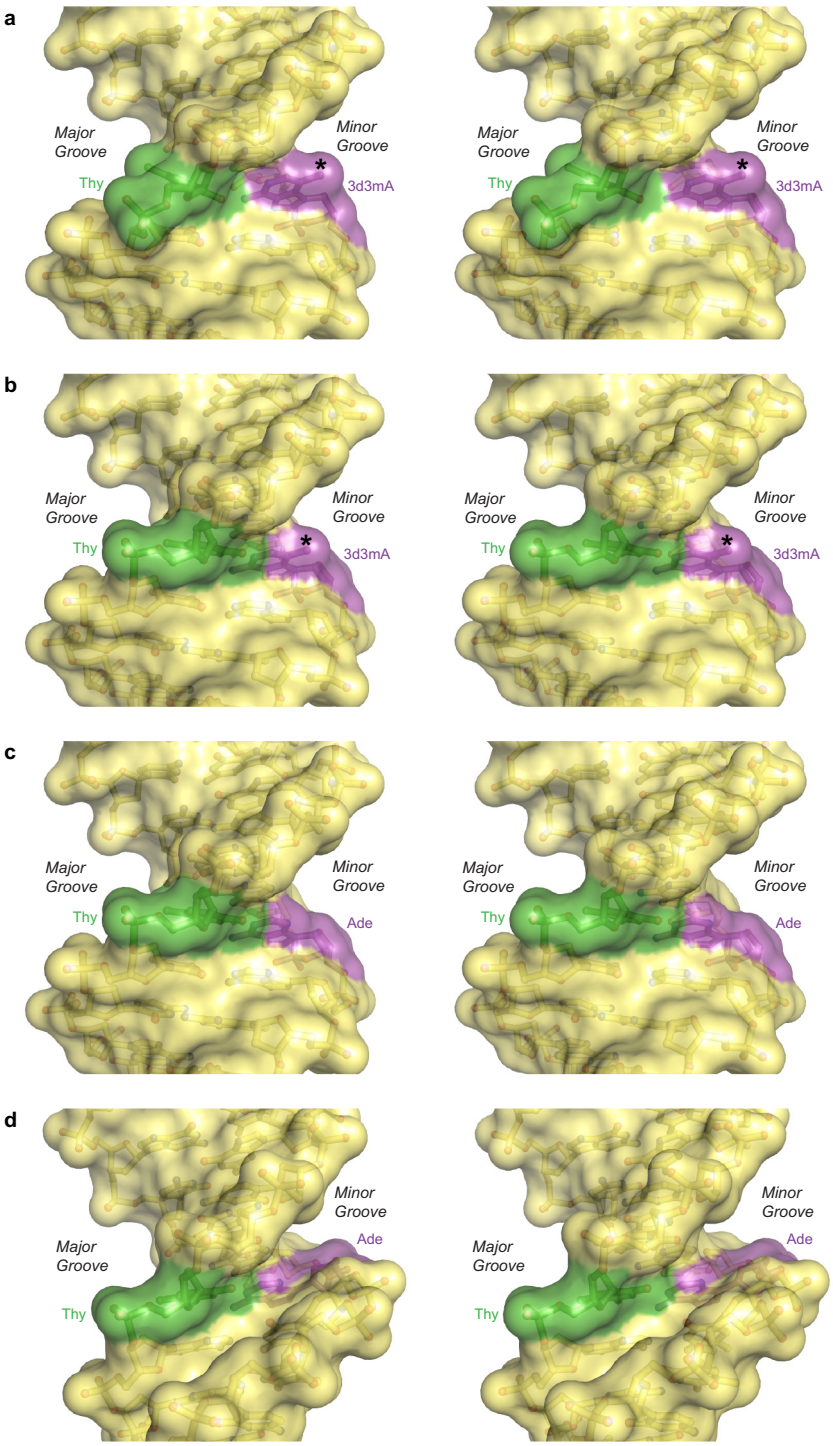

Extended Data Figure 1 | Remodelled DNA structures. DNA binding by AlkD bends the helical axis by 30° and widens the minor groove by 4 Å. Remodelling of this type reduces the energetic barrier to base pair opening but does not force base flipping[54–56]. In the AlkD–3d3mA-DNA complex, this distortion creates an equilibrium between Watson–Crick and sheared conformations of the 3d3mA•T base pair. In the sheared conformation, the 3d3mA nucleobase is displaced by 4 Å into the widened minor groove but remains partially stacked in the DNA duplex. **a**, Sheared 3d3mA•T base pair in the AlkD–DNA complex. **b**, Watson–Crick 3d3mA•T base pair in the AlkD–DNA complex. **c**, Simulated Watson–Crick A•T base pair in the AlkD–DNA complex. Adenine was generated by removing the methyl substituent from 3d3mA and changing carbon to nitrogen at the 3-position. Computational optimization was not performed. **d**, Watson–Crick A•T base pair in B-form DNA (PDB accession 1BNA). The asterisks in **a** and **b** indicate the position of the methyl substituent at *C*3. All structures are depicted as stereo images.

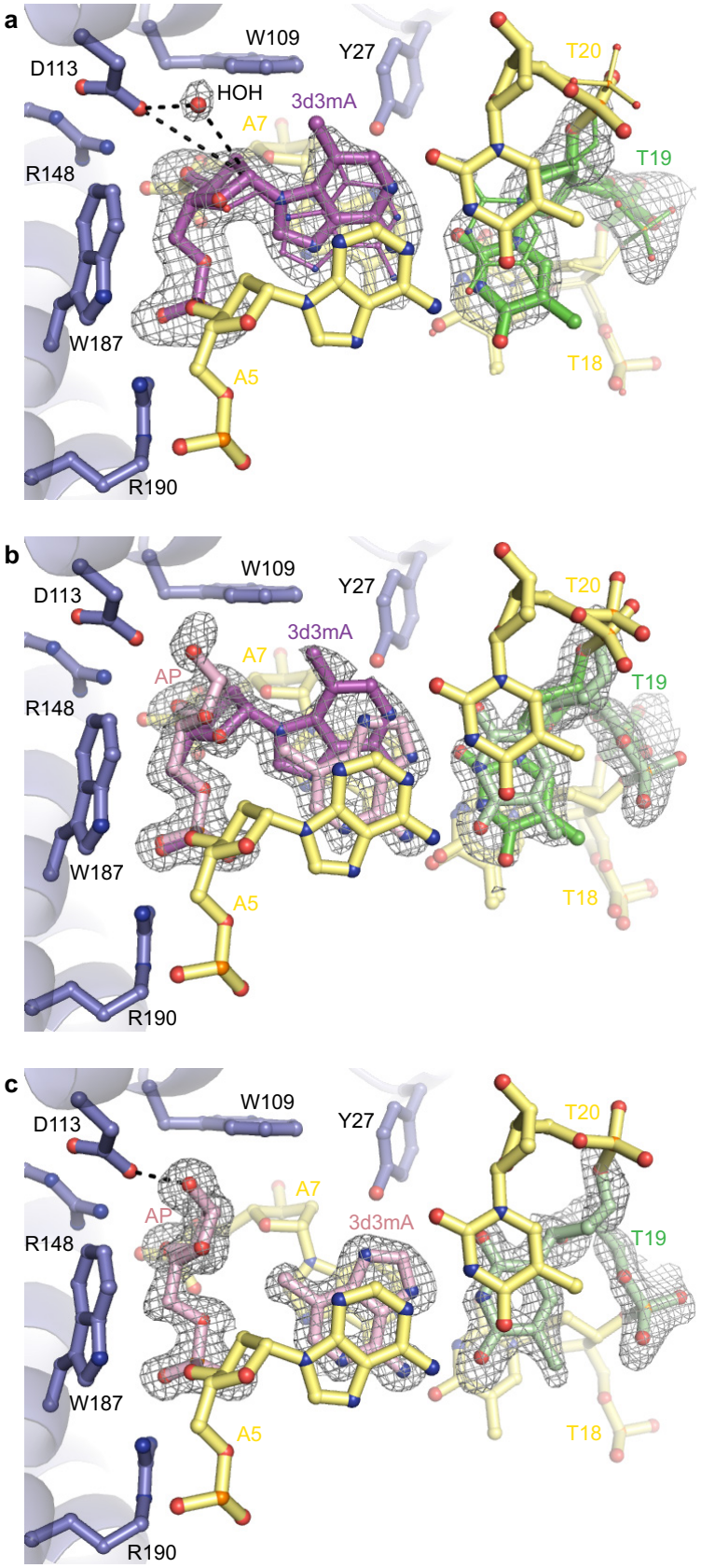

Extended Data Figure 2 | 3d3mA substrate and product structures. The AlkD–3d3mA-DNA complex was crystallized under moderately acidic (pH 5.7) conditions, causing a small fraction (~1%) of 3d3mA to become protonated and activated for enzymatic excision. Reaction progress was monitored by flash-freezing crystals at various times after preparing the protein–DNA complex and refining the fractional occupancies of substrate and product in the structures. **a**, Structure after 4 h containing only 3d3mA-DNA substrate. The 3d3mA•T base pair is present as a mixture of Watson–Crick (thin bonds) and sheared (thick bonds) conformations. **b**, Structure after 48 h containing a mixture of 3d3mA-DNA substrate together with AP-DNA product and 3d3mA nucleobase. **c**, Structure after 360 h containing only AP-DNA product and 3d3mA nucleobase. All panels show annealed omit electron density contoured to 2.5σ.

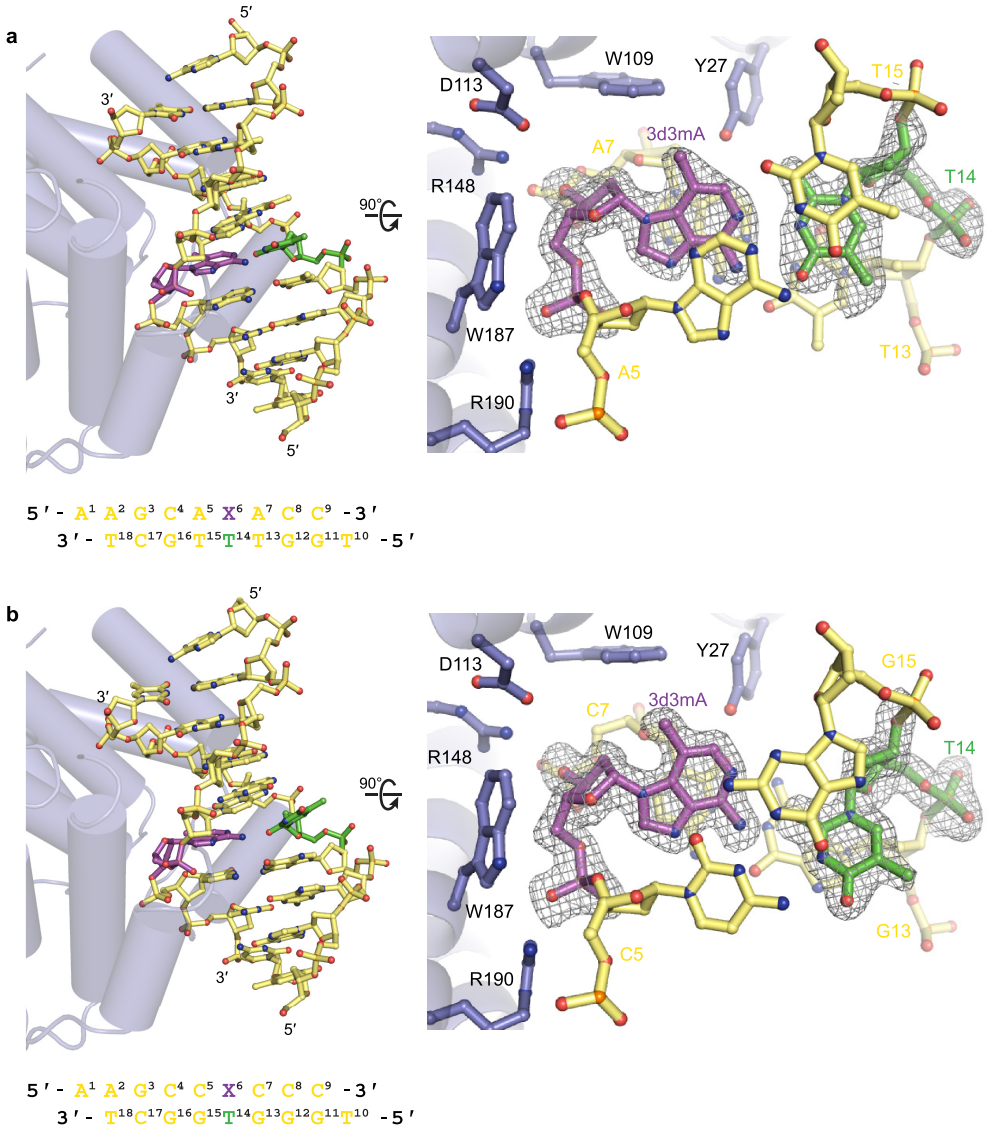

Extended Data Figure 3 | Additional substrate structures. AlkD was crystallized with two alternate 9-mer 3d3mA-DNA constructs to verify that crystal packing contacts were not significantly influencing the conformation of the DNA. As in the catalytic 12-mer substrate complex, 3d3mA remained stacked in the duplex in both 9-mer structures. However, unlike in the 12-mer complex, a mixture of Watson–Crick and sheared conformations was not observed. Instead, the 3d3mA•T base pair in each construct is either entirely in the Watson–Crick conformation or entirely in the sheared conformation. Formation of the AP product was not observed in either 9-mer construct, probably as a consequence of the neutral (pH 7.0) crystallization conditions, under which the fraction (<0.1%) of 3d3mA activated for depurination would be drastically reduced. **a**, Watson–Crick conformation. **b**, Sheared conformation. Both panels show annealed omit electron density contoured to 2.5σ.

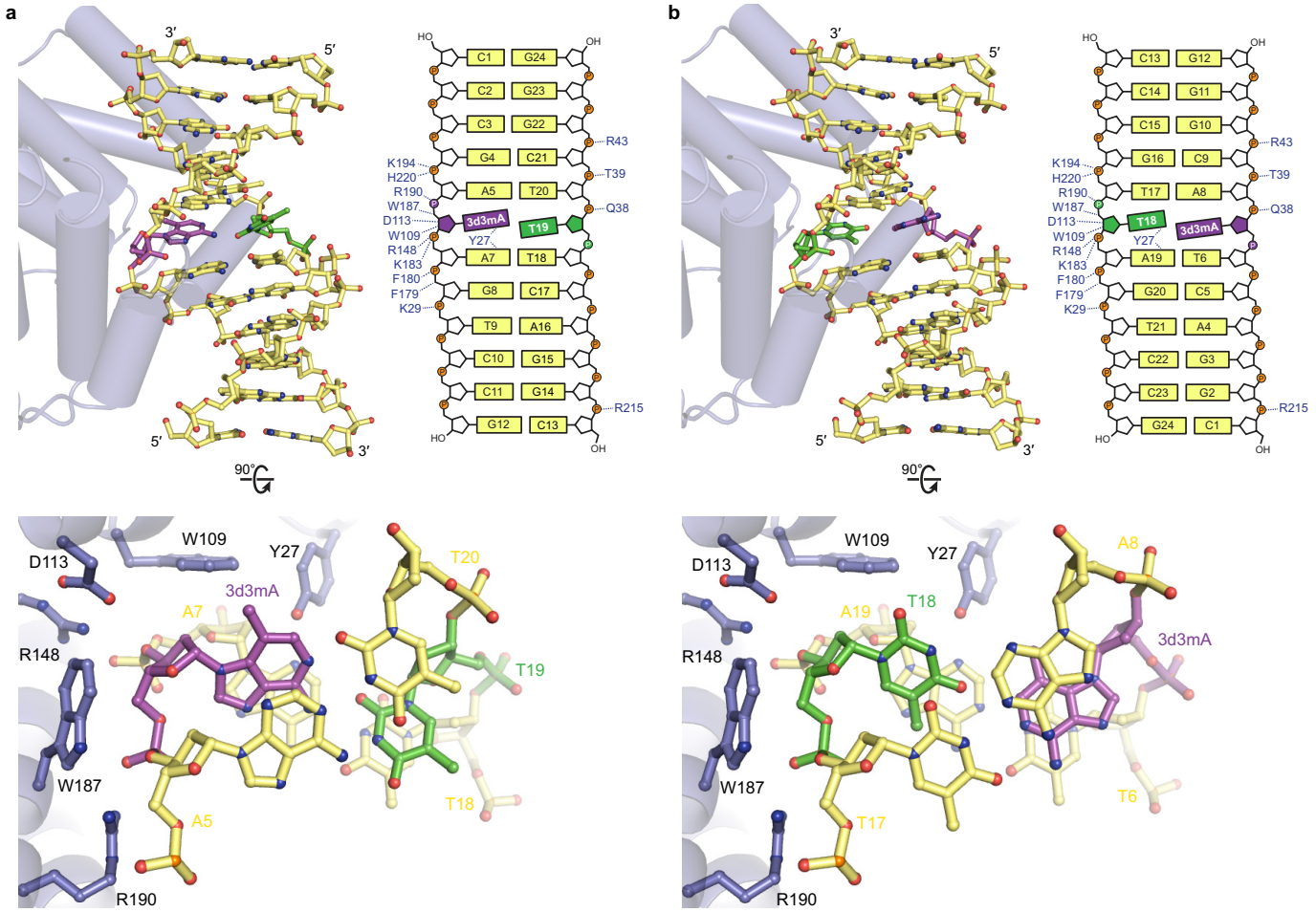

Extended Data Figure 4 | Comparison of catalytic and non-catalytic AlkD–3d3mA-DNA complexes. AlkD binds 3d3mA-DNA in two orientations that differ only in the position of the 3d3mA•T base pair about its dyad axis. Either 3d3mA (catalytic complex) or the opposing thymine (non-catalytic complex) resides against the protein surface. Both orientations use a common set of interactions that induce bending of the helical axis and widening of the minor groove, causing shearing of the 3d3mA•T base pair. In either complex, the nucleotide adjacent to the protein surface shows the same degree of displacement into the minor groove. The asymmetric position of the 3d3mA nucleotide in the duplex allows crystal packing interactions to select for a single orientation from a likely mixture of orientations in solution. Different DNA constructs were used to exploit these packing interactions and crystallize complexes in each binding orientation separately. Positive charge on the deoxyribose of 3mA would produce stronger electrostatic interactions with Trp109, Asp113 and Trp187 that would likely favour the catalytic binding orientation as well as a sheared conformation of a 3mA•T base pair. **a**, Catalytic orientation. The Watson–Crick conformer of the 3d3mA•T base pair was omitted for clarity. **b**, Non-catalytic orientation (PDB accession 3JX7).

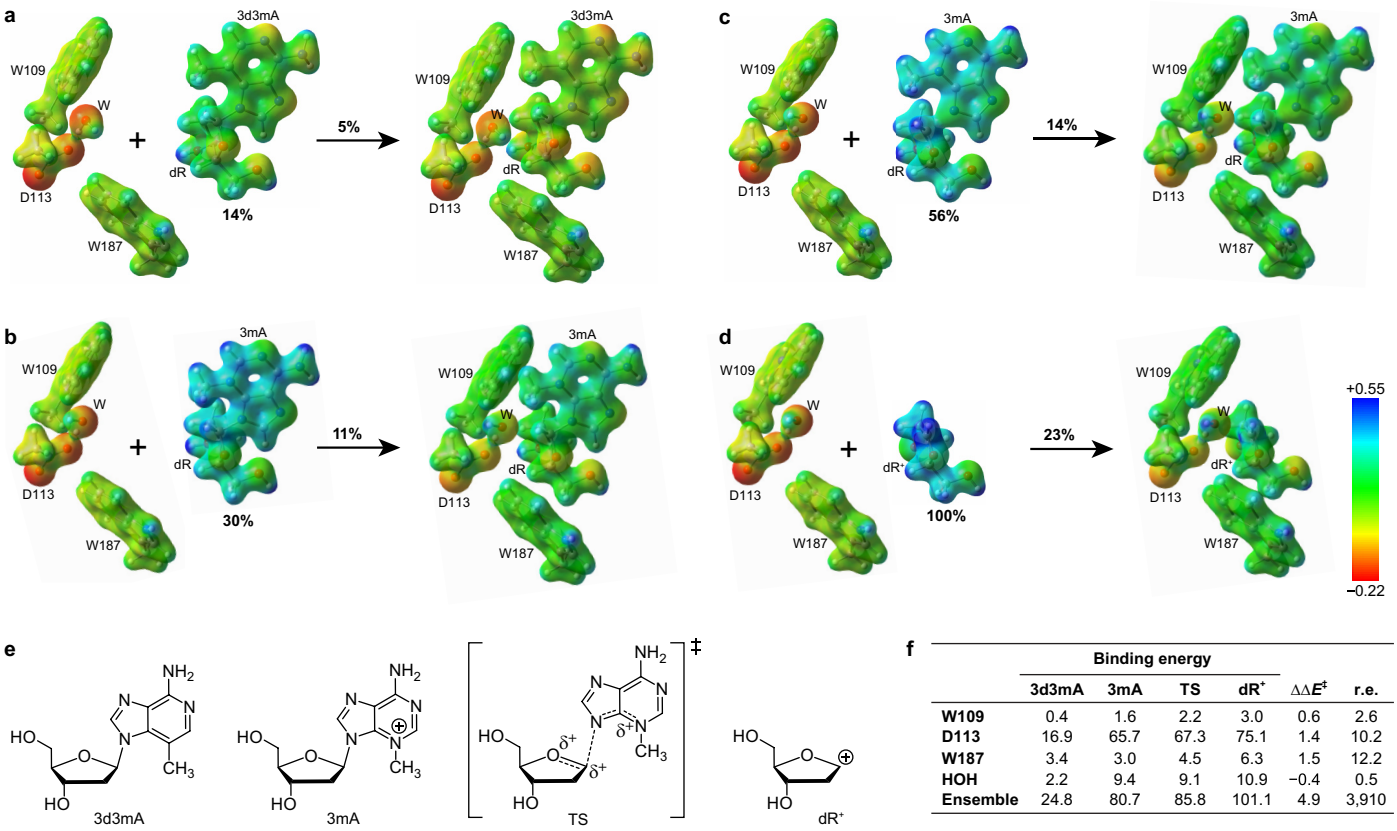

f

	Binding energy					
	3d3mA	3mA	TS	dR$^+$	$\Delta\Delta E^{\ddagger}$	r.e.
W109	0.4	1.6	2.2	3.0	0.6	2.6
D113	16.9	65.7	67.3	75.1	1.4	10.2
W187	3.4	3.0	4.5	6.3	1.5	12.2
HOH	2.2	9.4	9.1	10.9	−0.4	0.5
Ensemble	24.8	80.7	85.8	101.1	4.9	3,910

Extended Data Figure 5 | Electrostatic potential surfaces and computed binding energies. Charge transfer from the catalytic ensemble (Trp109, Asp113, Trp187 and Asp113-associated water) to the modified nucleosides stabilizes the AlkD–DNA complexes. **a**, 3d3mA substrate. **b**, 3mA substrate. **c**, Transition state (TS) approximation. **d**, dR$^+$ intermediate. Positive charge located on the deoxyribose moiety of the unbound nucleosides relative to that on the unbound dR$^+$ intermediate is indicated below the lesions. Charge transferred from the catalytic ensemble to the lesions upon complex formation is indicated above the arrows. Electrostatic potentials were scaled to −0.22–0.55 atomic units on an isodensity surface of 0.05 electrons bohr^{-3}. **e**, Modified nucleosides shown in **a**–**d**. **f**, Computed binding energies (kcal mol^{-1}), differential bond elongation energies ($\Delta\Delta E^{\ddagger}$, kcal mol^{-1}), and corresponding rate enhancements (r.e.).

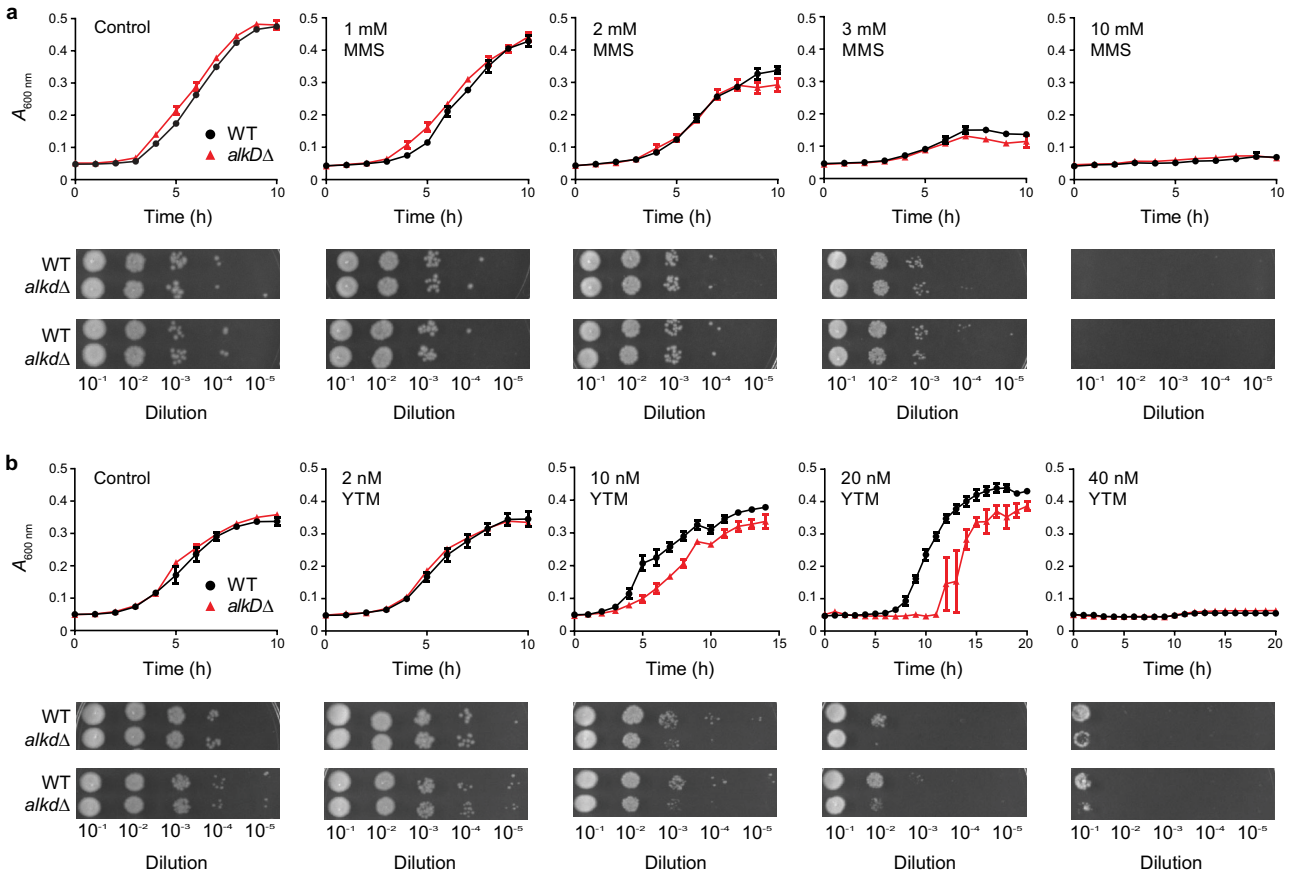

Extended Data Figure 6 | Growth curves and spot assays. Wild-type (black) and *alkD*-knockout (red) strains of *B. anthracis* were treated with varying concentrations of MMS and YTM. Control experiments contained no drug. Deletion of AlkD caused no observable phenotype with MMS but resulted in increased sensitivity to YTM. **a**, MMS treatment. **b**, YTM treatment. Error bars represent the s.e.m. from three replicate growth curves. Spot assays were performed in duplicate.

Extended Data Table 1 | X-ray data collection and refinement statistics

	3d3mA•T-DNA 100% substrate 4 hours	3d3mA•T-DNA AP•T-DNA/3d3mA 71% substrate/29% product 24 hours	3d3mA•T-DNA AP•T-DNA/3d3mA 51% substrate/49% product 48 hours	3d3mA•T-DNA AP•T-DNA/3d3mA 33% substrate/67% product 72 hours
Data collection				
Space group	$P2_1$	$P2_1$	$P2_1$	$P2_1$
Cell dimensions				
a, *b*, *c* (Å)	38.19, 93.65, 48.08	38.25, 93.56, 47.98	38.34, 93.40, 48.12	38.39, 93.28, 48.08
α, *β*, *γ* (°)	90.00, 113.05, 90.00	90.00, 112.74, 90.00	90.00, 112.85, 90.00	90.00, 112.72, 90.00
Resolution (Å)	50.00–1.97 (2.04–1.97)*	50.00–1.88 (1.95–1.88)	50.00–1.57 (1.60–1.57)	50.00–1.54 (1.57–1.54)
R_{merge}	0.068 (0.521)	0.084 (0.590)	0.063 (0.422)	0.058 (0.184)
Avg. $I/\sigma I$	18.4 (2.9)	18.4 (3.2)	21.3 (3.1)	34.0 (10.3)
Completeness (%)	99.8 (99.5)	99.9 (99.9)	99.9 (98.9)	99.4 (93.9)
Redundancy	4.1 (4.0)	5.3 (4.5)	4.2 (3.7)	7.5 (6.8)
Refinement				
Resolution (Å)	40.01–1.97 (2.06–1.97)	35.28–1.87 (1.94–1.87)	35.34–1.57 (1.61–1.57)	35.06–1.54 (1.58–1.54)
No. reflections	21,918 (2,701)	25,801 (2,791)	43,431 (3,010)	45,847 (3,225)
R_{work}	0.156 (0.217)	0.153 (0.216)	0.158 (0.208)	0.153 (0.169)
R_{free}†	0.189 (0.305)	0.196 (0.267)	0.189 (0.238)	0.183 (0.211)
No. atoms				
Protein	1,951	1,951	1,951	1,951
DNA	487	487	487	488
Water	177	207	356	413
Avg. *B*-factors‡ (Å^2)				
Protein	28.5	27.7	15.7	18.4
DNA	50.1	46.2	34.0	38.0
Water	39.0	38.6	31.8	35.2
R.m.s. deviations				
Bond lengths (Å)	0.007	0.007	0.006	0.006
Bond angles (°)	0.990	1.021	1.052	1.043
Ramachandran distribution (%)				
Favored	97.8	97.8	97.4	97.8
Allowed	2.2	2.2	2.6	2.2
Disallowed	0.0	0.0	0.0	0.0
PDB accession code	5CL3	5CL4	5CL5	5CL6

*Statistics for the highest resolution shell are shown in parentheses.
†R_{free} was determined from the 5% of reflections excluded from refinement.
‡Equivalent isotropic *B*-factors were calculated in conjunction with TLS-derived anisotropic *B*-factors.

Extended Data Table 2 | X-ray data collection and refinement statistics

	3d3mA•T-DNA AP•T-DNA/3d3mA 18% substrate/82% product 96 hours	AP•T-DNA/3d3mA 100% product 144 hours	AP•T-DNA/3d3mA 100% product 240 hours	AP•T-DNA/3d3mA 100% product 360 hours
Data collection				
Space group	$P2_1$	$P2_1$	$P2_1$	$P2_1$
Cell dimensions				
a, *b*, *c* (Å)	38.39, 93.15, 48.20	38.50, 93.45, 48.77	37.90, 92.87, 48.92	38.43, 93.08, 48.05
α, *β*, *γ* (°)	90.00, 112.81, 90.00	90.00, 114.19, 90.00	90.00, 113.77, 90.00	90.00, 112.61, 90.00
Resolution (Å)	50.00–1.44 (1.46–1.44)*	50.00–1.38 (1.40–1.38)	50.00–1.54 (1.57–1.54)	50.00–1.54 (1.60–1.54)
R_{merge}	0.069 (0.509)	0.047 (0.318)	0.050 (0.523)	0.049 (0.138)
Avg. $I/\sigma I$	23.3 (3.5)	31.9 (5.1)	32.0 (3.0)	41.1 (16.6)
Completeness (%)	96.4 (93.8)	99.5 (96.1)	99.5 (94.3)	96.9 (92.3)
Redundancy	6.4 (6.1)	7.3 (5.2)	6.2 (4.8)	7.7 (7.4)
Refinement				
Resolution (Å)	35.40–1.44 (1.47–1.44)	35.13–1.38 (1.41–1.38)	35.03–1.54 (1.58–1.54)	35.05–1.54 (1.58–1.54)
No. reflections	54,660 (3,702)	64,110 (4,402)	45,352 (3,149)	44,651 (3,037)
R_{work}	0.128 (0.150)	0.133 (0.160)	0.160 (0.227)	0.148 (0.147)
R_{free}†	0.166 (0.216)	0.158 (0.231)	0.186 (0.268)	0.169 (0.194)
No. atoms				
Protein	1,951	1,951	1,951	1,951
DNA	488	488	488	488
Water	363	405	248	400
Avg. *B*-factors‡ (Å^2)				
Protein	17.0	18.2	26.6	16.2
DNA	38.1	39.7	53.6	35.1
Water	33.2	33.9	41.1	33.5
R.m.s. deviations				
Bond lengths (Å)	0.008	0.008	0.006	0.006
Bond angles (°)	1.219	1.157	0.972	1.041
Ramachandran distribution (%)				
Favored	98.3	98.3	97.8	97.9
Allowed	1.7	1.7	2.2	2.1
Disallowed	0.0	0.0	0.0	0.0
PDB accession code	5CL7	5CL8	5CL9	5CLA

*Statistics for the highest resolution shell are shown in parentheses.
†R_{free} was determined from the 5% of reflections excluded from refinement.
‡Equivalent isotropic *B*-factors were calculated in conjunction with TLS-derived and individual anisotropic *B*-factors.

Extended Data Table 3 | X-ray data collection and refinement statistics

	3d3mA•T-DNA 9-mer A	3d3mA•T-DNA 9-mer B	1aR•T-DNA/3mA	THF•T-DNA/3mA
Data collection				
Space group	*C*2	*C*2	$P2_1$	$P2_1$
Cell dimensions				
a, *b*, *c* (Å)	127.44, 55.41, 47.97	127.40, 55.45, 47.56	38.20, 92.83, 48.31	38.49, 93.29, 48.16
α, *β*, *γ* (°)	90.00, 105.70, 90.00	90.00, 106.36, 90.00	90.00, 113.71, 90.00	90.00, 112.84, 90.00
Resolution (Å)	50.00–1.77 (1.83–1.77)*	50.00–1.73 (1.79–1.73)	50.00–1.54 (1.57–1.54)	50.00–1.73 (1.79–1.73)
R_{merge}	0.088 (0.414)	0.072 (0.362)	0.057 (0.255)	0.067 (0.443)
Avg. $I/\sigma I$	15.0 (2.7)	21.3 (5.1)	78.6 (7.0)	23.2 (3.4)
Completeness (%)	96.7 (80.0)	100.0 (99.9)	97.2 (92.2)	99.9 (99.6)
Redundancy	4.6 (4.2)	5.3 (4.8)	7.1 (6.4)	4.9 (4.6)
Refinement				
Resolution (Å)	46.20–1.77 (1.82–1.77)	45.65–1.73 (1.78–1.73)	35.00–1.54 (1.58–1.54)	40.09–1.73 (1.78–1.73)
No. reflections	30,638 (2,200)	33,412 (2,770)	44,194 (3,013)	32,539 (2,620)
R_{work}	0.163 (0.228)	0.154 (0.196)	0.149 (0.153)	0.155 (0.211)
R_{free}†	0.203 (0.277)	0.186 (0.252)	0.179 (0.179)	0.192 (0.288)
No. atoms				
Protein	1,898	1,898	1,951	1,951
DNA	364	364	487	487
Water	253	284	415	271
Avg. *B*-factors‡ (Å^2)				
Protein	24.2	23.6	14.6	21.2
DNA	38.3	32.2	33.1	39.5
Water	34.0	34.3	31.9	35.5
R.m.s. deviations				
Bond lengths (Å)	0.007	0.007	0.006	0.007
Bond angles (°)	1.030	1.074	1.049	1.009
Ramachandran distribution (%)				
Favored	97.7	97.3	97.9	97.8
Allowed	2.3	2.7	2.1	2.2
Disallowed	0.0	0.0	0.0	0.0
PDB accession code	5CLB	5CLC	5CLD	5CLE

*Statistics for the highest resolution shell are shown in parentheses.
†R_{free} was determined from the 5% of reflections excluded from refinement.
‡Equivalent isotropic *B*-factors were calculated in conjunction with TLS-derived anisotropic *B*-factors.